PHYSICAL REVIEW E **80**, 045301(R) (2009)

Spirals vortices in Taylor-Couette flow with rotating endwalls

M. Heise,* K. Hochstrate, J. Abshagen, and G. Pfister
Institute of Experimental and Applied Physics, University of Kiel, 24098 Kiel, Germany
(Received 19 June 2009; published 8 October 2009)

A Hopf bifurcation with translational invariance has been widely considered as an appropriate model for the appearance of spiral vortices in counter-rotating Taylor-Couette flow. Our experimental work demonstrates that flow conditions close to the axial boundaries are responsible for the type of bifurcation scenario, i.e., either asymmetric pure traveling waves or more complex behavior, such as defect states or symmetric mixed states appearing from a Hopf bifurcation. The measurements were performed in the first Taylor-Couette experiment with independently rotating endwalls confining the system in axial direction. The rotation rate of the (synchronous) endwalls is found to be an essential control parameter for the spatial amplitude distribution of the traveling waves and also reflects symmetry of the corresponding flow pattern appearing from the Hopf bifurcation.

DOI: 10.1103/PhysRevE.80.045301 PACS number(s): 47.20.Ky, 05.45.−a, 02.30.Oz

A realistic description of symmetry-breaking bifurcation events in a nonlinear extended system also includes symmetry-breaking imperfections as they are unavoidable in any physical realization [1,2]. A typical example arises from imperfections in reflection symmetric systems as they can be sufficiently captured by imperfect terms in pitchfork as well as in gluing bifurcations. Translational invariance is often assumed in a mathematical model of a bifurcation event in physical systems but it cannot be realized in an experimental system. As a typical example for a Hopf bifurcation with translational invariance serves the onset of spiral vortices in circular Couette flow (CCF) as a result of a linear instability [3–6]. CCF is the basic laminar state of Taylor-Couette flow, i.e., the flow of a viscous fluid in the gap between two concentric independently rotating cylinders, under the assumption of axial translational invariance [7]. In this case spiral vortices are traveling waves in axial and rotating waves in azimuthal directions [5,8]. More recently, it has been revealed that generic effects such as a Hopf bifurcation with broken translational symmetry appear [9,10]. In finite systems, i.e., experimental Taylor-Couette flow is typically confined by rigid axial endwalls, the translational invariance is always broken. However, observations of either upward or downward propagating spirals (SPIs) as the primary pattern have been interpreted in accordance with a Hopf bifurcation in counter- rotating CCF [6,11,12]. Numerous studies consider axial endwalls either as attached to the outer cylinder (see, e.g., [11–14]) or as nonrotating endwalls (see, e.g., [15,16]). Endwalls attached either to the outer or the inner cylinder was found to have influence on the stability of the flow [17]. Especially nonrotating endwalls subcritically innervate axisymmetric Ekman vortices in the annulus, leading to more complicated primary pattern consisting of both SPI structures, i.e., a left-handed spiral (L-SPI) and a right-handed spiral (R-SPI), in the bulk accompanied with defects near the Ekman vortices in the vicinity of the endwalls appears [16,18].

*heise@physik.uni-kiel.de

I. SYSTEM

The experimental setup consists of two concentric rotating cylinders (radii $r_{1,2}$; rotation rates $\Omega_{1,2}$) with a silicone oil of kinematic viscosity $\nu=10.6$ cS as working fluid in the gap ($d=r_2-r_1$) between them. The inner cylinder of the apparatus is machined from stainless steel having a radius of $r_1=(12.50\pm0.01)$ mm, while the outer cylinder is made from optically polished glass with a radius of $r_2=(25.00\pm0.01)$ mm. The temperature of the working fluid is thermostatically controlled to (24.00 ± 0.01) °C. At top and bottom, the fluid is confined by solid endwalls with a tilt of each plate being better than 0.03 mm. The endwalls are mechanically coupled to each other and therefore rotate synchronously. With a phase-locked-loop control, an accuracy of $10^{-4}(10^{-7})$ in the short (long) term average is achieved for the rotation rates of both cylinders and endwalls. Control parameters are the inner and the outer cylinder Reynolds numbers $R_{1,2}=r_{1,2}d\Omega_{1,2}/\nu$ and additionally the Reynolds number of the endwalls defined as $R_e=r_2d\Omega_e/\nu$. Geometric parameters are the aspect ratio $\Gamma=L/d$ and the radius ratio $\eta=r_1/r_2=0.5$. All lengths are scaled by the gap width d, times as well as frequencies by the diffusion time $\tau=d^2/\nu$ and velocities by d/τ. Throughout this Rapid Communication $R_2(=-120)$ as well as $\Gamma(=16)$ are held constant. However also measurements near these values have been performed.

II. MEASUREMENT TECHNIQUE

We utilize laser Doppler velocimetry (LDV) for measurements of the radial (u) and axial (w) velocity locally at any position (r,z,φ) within the flow domain. The measurements in this Rapid Communication have been performed at a fixed radial and azimuthal position (r,φ) while simultaneously axially moving the LDV at a constant speed w_{LDV} within the time t, i.e., each data point represents a certain time t referring to a distinct axial position $z(t)$. The corresponding evaluation algorithm is based on the occurring Doppler-shift using a bandpass filter that allows us to study the spatiotemporal behavior of stationary and oscillatory flow. In particu-

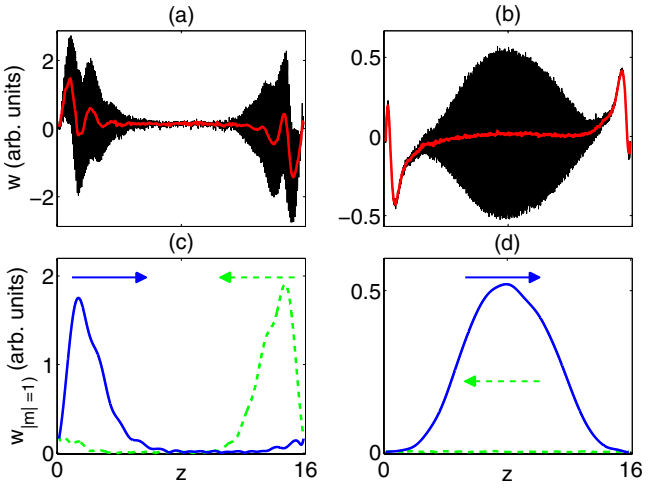

FIG. 1. (Color online) [(a) and (b)] Axial scans of two different spiral structures both recorded at $R_2=-120$ including the stationary part of the flow as red (gray) line. [(c) and (d)] Spatial amplitudes of each spiral mode L-SPI plotted as solid blue (dark gray) and R-SPI in dashed green (light gray) line both extracted by bandpass filtering from the corresponding axial scan in (a) and (b), respectively. The propagation direction of the corresponding spiral mode is indicated by the colored arrows. Parameters are $R_1=113$ and $R_e=60$ in (a) and (c) and $R_1=116$ and $R_e=-120$ in (b) and (d).

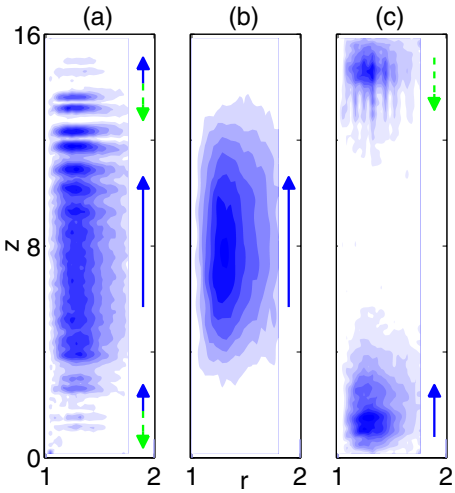

FIG. 2. (Color online) Experimentally determined radial velocity amplitudes of the spirals $u_{|m|=1}$ in the (r,z) plane at three different R_e, i.e., (a) stationary ($R_e=0$, $R_1=116$), (b) negative ($R_e=-120$, $R_1=116$), and (c) positive ($R_e=+60$, $R_1=113$). The blue (dark gray) color represents a high amplitude, whereas white represents an amplitude of zero. The propagation of the phase of each spiral in axial direction is additionally indicated by the dashed (R-SPI) and solid (L-SPI) colored arrows.

lar the (narrow) bandpass filtering of the so-called "axial scans" allows us to decompose the (spatial) time series into stationary pattern and axially traveling waves, e.g., axisymmetric Ekman vortices and nonaxisymmetric spiral vortices (see [19] for details).

III. SPIRAL STRUCTURE

Two characteristic examples of axial scans and the subsequent Doppler-based bandpass decomposition is depicted in Fig. 1. The axial scans and spatial amplitudes of spiral structures in the case of corotation, i.e., the endwalls and the inner cylinder rotate in the same direction, are depicted in Figs. 1(a) and 1(c). The axial scan in Fig. 1(a) reflects the superposition of a temporally stationary spatial pattern and a temporally oscillatory spatial pattern. The temporally stationary pattern appears as a peak in the power spectrum of the axial scan at a frequency given by the ratio between the speed of the LDV measurement position and the wavelength of the stationary spatial pattern. The other peaks corresponding to upward propagating L-SPI and downward propagating R-SPI patterns are slightly separated due to the Doppler shift caused by the downward-moving LDV measurement position. Once the proper frequencies are determined from the power spectrum, a narrow-band filter can be applied to separate the stationary Ekman profile [red (gray) line in Fig. 1(a)] and the two countermoving spiral patterns [colored lines in Fig. 1(c)]. The spatial amplitude of the upward propagating L-SPI (azimuthal wave number $m=+1$) is indicated by solid blue (dark gray) line and the downward propagating R-SPI ($m=-1$) is indicated by dashed green (light gray) line. Note that these spatial amplitudes are estimated by the envelope of the bandpass filtered axial scan. Additionally the propagation of the phase of each spiral in axial direction is indicated by the dashed and solid colored arrows, i.e., the phase propagates from the endwalls into the bulk. The upward propagating L-SPI mode is mainly located near the lower lid, whereas R-SPI is localized at the upper. In the bulk of the system no spiral amplitude is present. As is common for all type of spirals observed in counter-rotating Taylor-Couette flow until now, the defects near the both endwalls include an axisymmetric ($m=0$) mode on the one hand and both spiral modes ($m=\pm 1$) on the other hand [16,18].

Figures 1(b) and 1(d) show a different spiral structure observed when the endwalls and the outer cylinder are having the same rotation rate, i.e., $R_e=R_2=-120$, both counter rotating to the inner cylinder ($R_1=116$). For these parameters a pure (either upward or downward propagating) spiral mode, here L-SPI appears from Hopf bifurcation breaking the reflection symmetry of the flow. The main feature of this flow is the absence of the so-called Ekman spiral defects near the endwalls [20], where the corresponding other spiral mode, i.e., R-SPI($m=-1$), is zero in this case.

Figure 2 depicts the radial velocity amplitude distributions of the spirals $u_{|m|=1}$ for the three different R_e each resulting from successive axial scans of the radial velocity at 26 different radial positions in the gap between the counter-rotating cylinders. These three diagrams illustrate the spiral amplitude of the flow for three characteristic R_e values, i.e., zero, a negative and a positive value. To allow comparison between these results R_1 is always one Reynolds number above onset. The blue (dark gray) color represents a high amplitude, whereas white represents an amplitude of zero. Additionally the propagation of the phase of each spiral in axial direction is additionally indicated by the solid (L-SPI) and dashed (R-SPI) colored arrows.

The distribution depicted in Fig. 2(a) represents the case of stationary endwalls. It results from an upward traveling

L-SPI breaking the reflection symmetry of the flow especially in the bulk. Note that the respective state with a downward traveling spiral has also been observed. The radial amplitude of the spiral is dominant in the bulk of the system and disappears near both endwalls. However, also the distribution is asymmetric because the Ekman spiral defects occur at each end with phase generation and annihilation at top and bottom, respectively. These defects include an axisymmetric Ekman induced mode as well the amplitude of both nonaxisymmetric spiral modes (L-SPI and R-SPI). The distribution illustrated in Fig. 2(b) is recorded at $R_e=-120$, i.e., for the corotating case as partly shown in Figs. 1(b) and 1(d) and results also from an upward traveling L-SPI. The amplitude is spatially distributed over the entire gap but the maximum is located in the axial midplane of the system while it is decreasing toward the upper and lower lids. Due to the phase propagation of the spiral from bottom to top the flow is asymmetric in axial direction but the amplitude distribution is almost symmetric. Note that in contrast to the distribution in Fig. 2(a) the R-SPI mode is not existent near the endwalls or the bulk.

The spiral structure can change qualitatively in the case of positive R_e as the amplitude distribution in Fig. 2(c) illustrates. The main difference with respect to the other two distributions is the symmetric appearance of amplitude in the vicinity of both endwalls. Moreover, at the upper lid R-SPI appears whereas at the lower one L-SPI, i.e., the reflection symmetry of the flow is preserved. Hence R_e thereby serves as control parameter to either break or preserve this reflection symmetry of the Hopf bifurcation.

IV. BIFURCATION BEHAVIOR

In order to characterize the transition from basic flow to the spirals, an experimental bifurcation diagram is displayed in Fig. 3(a) for $R_e=120$. As a measure for the bifurcation event the squared spiral amplitude $\langle w_{|m|=1}\rangle^2$ is plotted versus R_1. Each point (∘) results from the mean amplitude of a time series which is recorded at the axial middle of the system and a radial distance of $0.2d$ from the inner cylinder. During the scenario R_1 is quasistatically increased in steps of $\Delta R_1=0.2$ and each time series has a length of 22τ. The onset of the corresponding spiral (vertical dashed line) and a linear fit considering the amplitude values above the corresponding onset (solid line) are indicated in this plot. Together with a finite oscillation frequency the linear relationship between the squared spiral amplitude $\langle w_{|m|=1}\rangle^2$ with respect to R_1 the transition to the spirals can be characterized in form of a supercritical Hopf bifurcation. This bifurcation behavior has also been proofed for other R_e and does not change qualitatively in the parameter regime considered here ($-130\leq R_e\leq+130$).

In Fig. 3(b) an experimentally determined stability diagram of the basic flow is depicted, where the inner Reynolds number R_1 for the onset of the spiral is plotted versus R_e. The onset of the spirals (∘ and solid line) as well as the critical $R_{1,c}=115.03$ resulting from linear stability analysis of CCF (dashed line) is included in this diagram. It is in excellent agreement for the onset of the spirals in particular for stationary and negative values of R_e. Also for positive R_e it is in good agreement but within the interval R_e ($+44\leq R_e\leq+76$), where a significant difference between the values resulting from linear stability analysis is visible with the lowest value at $R_1=110.6$, i.e., $\Delta R_1\approx 5$ below linear instability of CCF. In Fig. 3(c) the experimentally determined oscillation frequencies of the spirals (∘) are plotted versus R_e. For comparison also the oscillation frequency resulting from linear stability of CCF (f_{lin}) is indicated as dashed line. They vary only slightly with R_e and the one obtained from experiment are in very good agreement (<1%) to the one from linear stability analysis.

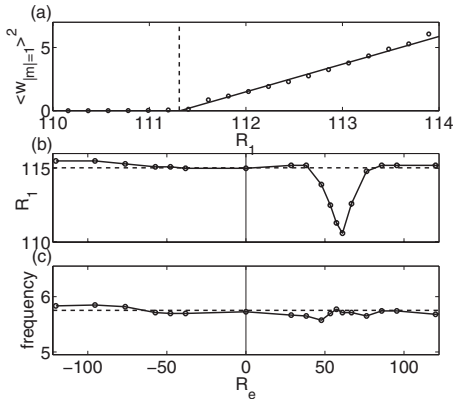

FIG. 3. (a) Bifurcation diagram recorded at $R_2=-120$, $R_e=+120$, and $r=r_1+0.2d$ in the axial middle of the system. The squared spiral amplitude $\langle w_{|m|=1}\rangle^2$ is plotted versus R_1. The onsets of the spiral is indicated by the vertical dashed lines and the solid lines are a linear fit of the oscillation amplitude above onset. (b) Stability diagram of the basic flow with respect to R_e. The markers (∘) indicate the onset of the oscillatory flow in experiment and the solid line connects these measured values to guide the eyes. In addition to that the critical $R_{1,c}$ resulting from linear stability analysis for the case of infinite long cylinders is plotted as dashed line. (c) Oscillation frequencies at onset (∘) versus R_1.

V. FLOW NEAR ENDWALLS

In order to understand the differences in flow pattern above onset it is essential to characterize the basic flow slightly below. Thus the radial and the axial velocity fields (u,w) in the (r,z) plane together with the color coded axial velocity field of the spiral structure is depicted in Fig. 4 for three different R_e slightly below the respective onset of spirals ($\Delta R_1=1$). Note that due to the symmetry of the basis flow only the lower half of the flow domain is depicted.

The measurement of the basic flow for stationary endwalls ($R_e=0$, $R_1=114$) is shown in Fig. 4(a). An axial column of three vortices located near the lower endwall are visible is this measurement. The amplitude of those Ekman induced vortices decreases with respect to the distance to the lower endwall. That behavior is in agreement with previous results including an inward directed flow at the lower endwall [19]. For negative R_e, i.e., in the same direction as the outer cylinder, ($R_e=-120$, $R_1=114$) the character of the basic flow changes qualitatively. Just one single large vortex is

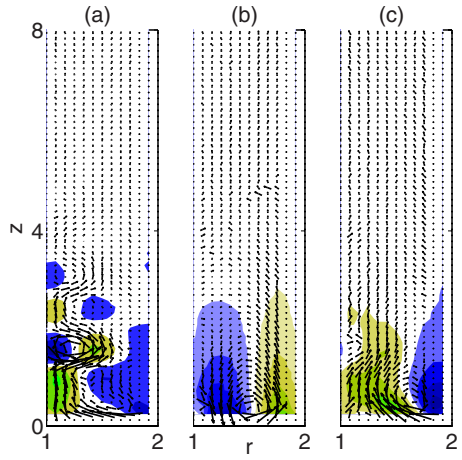

FIG. 4. (Color online) Experimentally measured radial (u) and axial (w) velocity field together with the color coded axial velocity w [blue (dark gray) represents a positive value, whereas green (light gray) represents a negative one] in the (r,z) plane for the basic flow at three different R_e, i.e., (a) stationary ($R_e=0$, $R_1=114$), (b) negative ($R_e=-120$, $R_1=114$), and (c) positive ($R_e=+60$, $R_1=109$).

visible in the corresponding measurement in Fig. 4(b). It can be seen that the flow is directed downward at the inner and upward at the outer cylinder and therefore directed outward at the lower (and the upper) endwall. For positive R_e, i.e., in the opposite direction as the outer cylinder, ($R_e=+60$, $R_1=109$) in Fig. 4(c) the behavior reverses with respect to the counter-rotating case: an inward directed flow at the endwalls occurs whereby the flow is directed upward at the inner and downward at the outer cylinder in the lower half of the cylinder. Moreover, the vortex structure differs to the one presented in (a) as only a single vortex instead of a column of small vortices exists.

VI. CONCLUSION

Our experimental study revealed the influence of endwalls rotation on the type of spiral flows appearing from the Hopf bifurcation in counter rotating Taylor-Couette flow. In particular we have shown that rotating endwalls retain the Hopf bifurcation of the basic flow but significantly alter the appearing flow pattern. Depending on R_e either pure spirals or more complicated mixed spiral flow pattern appear. Those mixed states either keep or break the reflection symmetry of the system and may contain defects. Therefore we conclude that the flow conditions near the endwalls determine Hopf bifurcation scenario in counter-rotating Taylor-Couette flow and thereby serves as a further control parameter allowing us to unfold the bifurcation, i.e., the rotation rate of the (synchronously) rotating endwalls.

ACKNOWLEDGMENT

We acknowledge support from the Deutsche Forschungsgemeinschaft.

[1] T. Mullin, *The Nature Of Chaos* (Oxford University Press, New York, 1993).
[2] M. Golubitsky and I. Stewart, SIAM J. Math. Anal. **17**, 249 (1986).
[3] H. Snyder, Phys. Fluids **11**, 728 (1968).
[4] E. Krueger, A. Gross, and R. Di Prima, J. Fluid Mech. **24**, 521 (1966).
[5] M. Golubitsky and W. Langford, Physica D **32**, 362 (1988).
[6] W. Langford, R. Tagg, E. Kostelich, H. Swinney, and M. Golubitzky, Phys. Fluids **31**, 776 (1988).
[7] R. Tagg, Nonlinear Sci. **4**, 2 (1994).
[8] P. Chossat and G. Iooss, *The Couette-Taylor Problem* (Springer, New York, 1994).
[9] J. Crawford and E. Knobloch, Nonlinearity **1**, 617 (1988).
[10] J. Langenberg, G. Pfister, and J. Abshagen, Phys. Rev. E **68**, 056308 (2003).
[11] D. Coles, J. Fluid Mech. **21**, 385 (1965).
[12] C. Andereck, S. Liu, and H. Swinney, J. Fluid Mech. **164**, 155 (1986).
[13] W. Edwards, R. Tagg, B. Dornblaser, and H. Swinney, Eur. J. Mech. B/Fluids **10**, 205 (1991).
[14] G. Taylor, Proc. R. Soc. London, Ser. A **223**, 289 (1923).
[15] J. Abshagen, M. Heise, J. Langenberg, and G. Pfister, Phys. Rev. E **75**, 016309 (2007).
[16] C. Hoffmann, M. Lücke, and A. Pinter, Phys. Rev. E **72**, 056311 (2005).
[17] H. Snyder, Phys. Fluids **11**, 1599 (1968).
[18] M. Heise, D. Küter, J. Abshagen, and G. Pfister, J. Phys.: Conf. Ser. **137**, 012004 (2008).
[19] M. Heise, J. Abshagen, D. Küter, K. Hochstrate, G. Pfister, and Ch. Hoffmann, Phys. Rev. E **77**, 026202 (2008).
[20] M. Heise, C. Hoffmann, J. Abshagen, A. Pinter, G. Pfister, and M. Lücke, Phys. Rev. Lett. **100**, 064501 (2008).